Plasmo-thermomechanical suspended nanowire array detectors for mid-infrared spectrum

Conference Paper · August 2017

DOI: 10.1117/12.2274483

6 authors, including:

Mohammad Wahiduzzaman Khan
University of California, Irvine
6 PUBLICATIONS **3** CITATIONS
SEE PROFILE

Parinaz Sadri-Moshkenani
University of California, Irvine
5 PUBLICATIONS **3** CITATIONS
SEE PROFILE

Rasul Torun
University of California, Irvine
16 PUBLICATIONS **65** CITATIONS
SEE PROFILE

Ozdal Boyraz
University of California, Irvine
176 PUBLICATIONS **2,664** CITATIONS
SEE PROFILE

PROCEEDINGS OF SPIE

SPIEDigitalLibrary.org/conference-proceedings-of-spie

Plasmo-thermomechanical suspended nanowire array detectors for mid-infrared spectrum

Qiancheng Zhao
Mohammad Wahiduzzaman Khan
Parinaz Sadri-Moshkenani
Rasul Torun
Imam-Uz Zaman
Ozdal Boyraz

SPIE.

Plasmo-thermomechanical suspended nanowire array detectors for mid-infrared spectrum

Qiancheng Zhao, Mohammad Wahiduzzaman Khan, Parinaz Sadri-Moshkenani, Rasul Torun, Imam-Uz Zaman, and Ozdal Boyraz*

Department of Electrical Engineering and Computer Science, University of California, Irvine, CA, USA, 92697

**oboyraz@uci.edu*

ABSTRACT

We propose a plasmo-thermomechanical mid-infrared detector operating at 4.3 μm wavelength. The design utilizes an array of the bimetallic fishbone nanowires that are suspended 50 nm above a 1.5 μm × 0.3 μm silicon nitride waveguide to create a leaky wave radiation. Moreover, the thermo-mechanically actuated nanowire will induce evanescent wave modulation that can be detected by the leaky wave or transmitted power of the waveguide. The antenna has a strip length of 1.77 μm and can yield an absorption coefficient of 42.4% with a period of 3.1 μm. Six unit cells are connected by a nanowire, and the fishbone-like nanowires are clamped at the two ends, leaving the center free to bend. The mid-infrared energy is absorbed by the resonant metallic antennas, resulting in a temperature increment. The mismatch of the thermal expansion coefficients of the bimetallic materials, gold and nickel, actuates the nanowire, and thus changes the gap between the nanowire and the waveguide. The deformation of the nanowire modulates the waveguide evanescent field, and hence alternates the transmitted power as well as the leak wave power. With a normal incident power of 4 $\mu W/\mu m^2$, the temperature in the center of the nanobridge can be increased over 135 K above the ambient temperature, leading to an elevation of 23.5 nm in the center and thus weakening the evanescent modulation strength. The difference of S_{21} caused by the gap change is 0.106. This methodology can be applied in other spectrums and the fabrication progress will be reported later.

Keywords: infrared detectors, bimetallic nanobeam, plasmonic antennas, thermoplasmonics, thermomechanics, SiN waveguide.

1. INTRODUCTION

Infrared detection relies on the energy transduction mechanism that transfers the electromagnetic energy into other formats. Depending on the energy transduction mechanism, most of the infrared detectors can be classified as either quantum and thermal detectors [1]. The thermoplasmonics, which takes advantage of the photo-thermal effect induced by the resonant light absorption in metallic nanostructures, has become an appealing direction in nanoscale heat sources [2], [3]. By tuning the plasmonic structures, high absorption coefficient can be achieved at different wavelengths depending on the antenna length [4], which renders the design of the plasmonic structure flexible and scalable. Heat transformed by the thermal generators induces the temperature change, and can be measured by the temperature-dependent mechanisms, which include pyroelectricity [5], thermoelectricity [6], conductivity [7], thermo-optics [8], [9], mechanical deflections [10]–[12], etc. Among these mechanical thermal detectors, bimaterial devices play an important role. The bimaterial thermal detectors usually utilize the cantilevers or the suspended membranes that deflect due to thermal expansion. To convert the tiny mechanical deflection into a measurable quantity, optical systems are often employed based on trigonometry [13]–[16] or interferometry [17], [18]. However, these optical systems require discrete bulky lenses and detectors, and hence the miniaturization of the detectors remains difficult.

Inspired by the metal-based evanescent field modulators [19] and our recent achievements of the optical leaky wave antennas (OLWAs) [20]–[22], here we propose an on-chip plasmo-thermomechanical detector for IR radiation [23], [24]. The merit of the design is to detect the radiation-induced mechanical deflection through a waveguided light, thus making

Infrared Sensors, Devices, and Applications VII, edited by Paul D. LeVan, Ashok K. Sood, Priyalal Wijewarnasuriya, Arvind I. D'Souza, Proc. of SPIE Vol. 10404, 104040L
 · doi: 10.1117/12.2274483

the bolometer compact and can be integrated on-chip. To be specific, the free space target IR radiation is absorbed by the fishbone nanowires and creates thermo-mechanical deflection on the suspended wires. The gap between the nanowires and the underneath waveguide is selected to have an evanescent field interaction that causes attenuation on the waveguided mode. Thus, the change in the target IR radiation intensity is read out by the attenuation on the transmitted power in the waveguides at the probe wavelengths, which can be easily realized by an on-chip photo detector. The proposed design embraces the capability for on-chip integration and the flexibility for operation due to the separation of the target and probe wavelengths. In particular, we show the optimized design for the target wavelength at 4.3 μm and the probe wavelength at 1550 nm. To assess the performance of the device, the figure of merit (FOM) is defined as the ratio of the change in S_{21} in the waveguide with respect to the illumination power density, namely $\Delta|S_{21}|/I_{IR}$, where I_{IR} is the IR power density in the unit of W/m^2. The figure of merits (FOMs) of the proposed device is 2.64×10^{-2} μm^2/μW.

2. DESIGN OF THE PLASMO-THERMOMECHANICAL DETECTOR

2.1 Device Structure

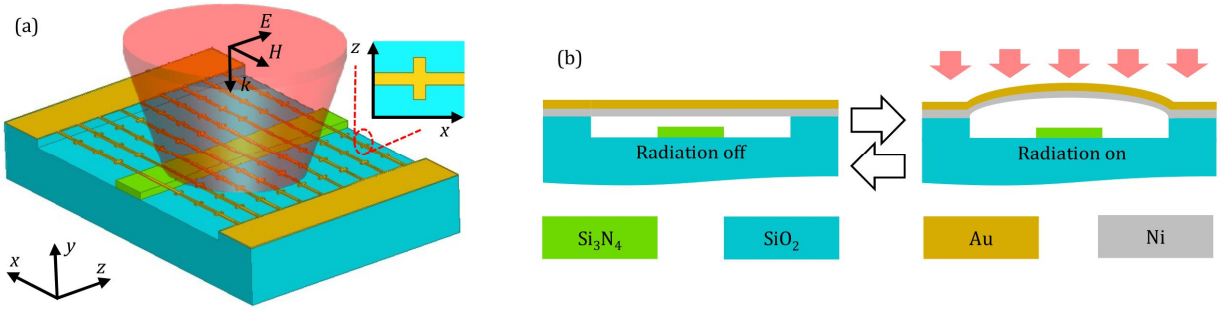

Figure 1. Schematic geometry (a) and operation principle (b) of the bilayer plasmo-thermomechanical detector for IR radiation. The inset in (a) shows the top view of the antenna unit cell.

As demonstrated in Figure 1(a), the operation of the detector needs the interplay of three key elements: strip antennas, bimetallic fishbone nanowires, and a waveguide. Silicon nitride (SiN) is chosen as the waveguide core material. SiN waveguides have been widely used in passive [25]–[31] and active [32]–[36] photonic devices. The inclusion of metallic structures equip SiN waveguides with the capabilities of enhancing evanescent field [37], [38] and generating hot spots [39]–[41]. Plasmonic metallic antennas can not only alter the wave delay [42] but also absorb electromagnetic energy when excited by the resonant wavelength. When the infrared energy is absorbed by the resonant metal strips, the absorbed energy is conducted to the nanowires and creates a thermal gradient. The temperature variation will thermally actuate the nanowires, changing the gap between the nanowires and the waveguide top surface, as illustrated in Figure 1(b). In our design, the deformation of the nanowires modulates the evanescent field from the waveguide whose dimension is 1.5 μm × 0.3 μm to guarantee the single TE mode at 1550 nm wavelength. The gap between the nanowires and the waveguide determines the strength of the interaction, which is set to be 50 nm, a separation that has enough evanescent field interaction, and that is also fabrication feasible, e.g., etching the silicon dioxide (SiO_2) sacrifice layer with hydrogen fluoride (HF) acid vapor. For the sake of fabrication compatibility, gold (Au) and nickel (Ni) are used to build the nanowires due to their chemical resistance to HF. Since Au has a larger thermal expansion coefficient than Ni, Au should be placed on top of Ni, so that the nanowire will bend upward to avoid collapsing and sticking to the waveguide surface. The amount of deflection of nanowires is determined by the relative thickness of each layer, the temperature gradient, and the length of the nanowire. In the following sessions, we show how to optimize the nanowires for maximum deflection and hence optical modulation on the propagating waves.

2.2 Thermomechanical Analysis and Simulation

The detection system is modeled and simulated in three parts, being the plasmo-thermal conversion, the thermo-mechanical deflection, and the evanescent field modulation. We use the finite element method based software (COMSOL Multiphysics) to solve all three parts. The composition of the nanowire is first settled by the thermo-mechanical simulation. Bilayer beams are widely used to sense and control the temperatures [13], [14]. Due to the difference of the thermal expansion coefficients of the materials, stress and constrains will be created, resulting in beam bending. The beam will bend towards the material with a larger thermal expansion coefficient when experiencing a

positive temperature difference, and bend towards the material with smaller thermal expansion coefficient if the beam is cooled.

The temperature-induced bending of the double clamped bilayer beam (inset in Figure 2) is a function of the thermal expansion coefficient γ, layer thickness t, and temperature profile $T(x)$ as described in Eq. (1) and (2) [43], [44]:

$$\frac{d^2\Delta y}{dx^2} = 6(\gamma_2 - \gamma_1)\frac{t_1 + t_2}{t_2^2 K}\left[T(x) - T_0\right] \tag{1}$$

$$K = 4 + 6\left(\frac{t_1}{t_2}\right) + 4\left(\frac{t_1}{t_2}\right)^2 + \frac{E_1}{E_2}\left(\frac{t_1}{t_2}\right)^3 \frac{1-\nu_2}{1-\nu_1} + \frac{E_2}{E_1}\left(\frac{t_2}{t_1}\right)\frac{1-\nu_1}{1-\nu_2} \tag{2}$$

where $\Delta y(x)$ is the vertical deflection of the beam at the position x and the origin is located at the center of the beam, E is the Young's modulus, ν is the Poisson's ratio. The subscripts 1 and 2 represent the top and the bottom layers. The ambient temperature is denoted by T_0. The material properties used in the simulations are summarized in the following table.

Table 1. Gold and nickel mechanical properties

	γ (10^{-6} /K)[45]	E (10^9 Pa)[46]	ν (dimensionless)[47]
Gold	14.2	78	0.44
Nickel	13.4	200	0.31

As formulated in Eq. (1), a thick wire may reduce the amount of deflection. However, if the wire is too thin, it may not have enough mechanical strength for suspension. Here, we set the wire thickness t_1+t_2 to be 50 nm as a tradeoff between the mechanical strength and the amount of deflection of the wire. Given a temperature profile $T(x) - T_0 = \Delta T\cdot(1-(2x/l)^2)$ where l is the length of the beam and ΔT is the temperature difference at the beam center, the amount of deflection is estimated to be

$$\Delta y(x) = 24(\gamma_2 - \gamma_1)\frac{t_1 + t_2}{t_2^2 K}\cdot\Delta T l^2\left(-\frac{1}{2}\left(\frac{x}{l}\right)^4 + \frac{1}{8}\left(\frac{x}{l}\right)^2 - \frac{5}{192}\right) \tag{3}$$

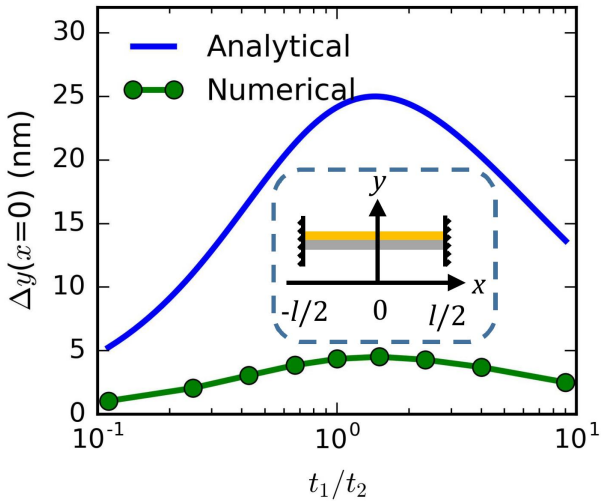

Figure 2. Comparison of the displacement in the center of the beam as a function of the top and bottom layer thickness ratio, t_1/t_2, using the analytical formula and the FEM simulation method. The inset shows the schematic of the double clamped bilayer beam.

Figure 2 illustrates the analytical and numerical estimation of the deformation for the Au and the Ni composed layers. In these calculations, we assume a beam length l = 10 μm, beam width W_b = 100 nm (for numerical analysis only), and ΔT

= 100 K. The shortcoming of the analytical method arises from the fact that it does not consider the wire width in calculation, and hence the analytical result is 5 times higher than the rigorous numerical analysis. This mismatch has also been explained in Ref. [16] and reported in the support information of Ref. [48]. Despite the discrepancy of the peak values, the analytical and numerical solutions agree well that the ratio of the Au and Ni layer thickness should be 1.5.

2.3 Design of the Fishbone Unit Cell

In our design, strip antennas are employed to absorb the infrared radiation and to generate thermal gradient. To increase the total absorbed energy, multiple antennas are connected by a single nanobeam, yielding a fishbone-like nanowire. The design of the fishbone nanowire is performed in unit cells, which repeat itself in the x and z directions. Although the periodicity breaks at the anchor supports, the simulation of the unit cell still acts as a good approximation of the electromagnetic behavior of the entire wire. The fishbone nanowire, surrounded by air, is suspended 350 nm above a SiO_2 substrate and stretches across the SiN waveguide. Its unit cell only contains the SiO_2 substrate in the model since the waveguide width is assumed to be narrower than the nanowire and can be ignored in the unit cell optimization stage. We set the substrate thickness to be 2λ and the air box thickness to be 3λ, where λ is the infrared wavelength in free space. Both the substrate and the air box are sandwiched in perfect matched layers (PMLs) to absorb scattering light and to minimize reflections at the top and bottom boundaries. The PML thickness is set to be λ. The optical properties of the materials at 4.3 μm wavelength are summarized in the following table.

Table 2. Optical properties of the air, SiN, SiO_2, Au and Ni that are used in the simulation.

Material	ε_r	μ_r	σ
Air	1	1	0
SiN	2	1	0
SiO_2	1.907 [49]	1	0
Au	-731.49 – j149.95[50]	1	45.6×10^6 [51]
Ni	-225.07 – j130.52 [50]	1	13.8×10^6 [51]

The unit cell (inset in Figure 3(b)) is optimized in terms of the strip length L_s, strip width W_s, and periods in the x and z directions. The beam width W_b is set to be 100 nm in our study. As shown in Figure 3(a), increasing the width of the strip will reduce the resonant length and lower the absorption coefficient. We find out that the combination of L_s = 1.77 μm and W_s = 100 nm yields the highest absorption coefficient at λ = 4.3 μm. The periods in the x and z directions are optimized simultaneously to achieve $P_x = P_z$. The absorption coefficient reaches a peak value of 0.424 when the periods equal 3.1 μm in both x and z directions as shown in Figure 3(b).

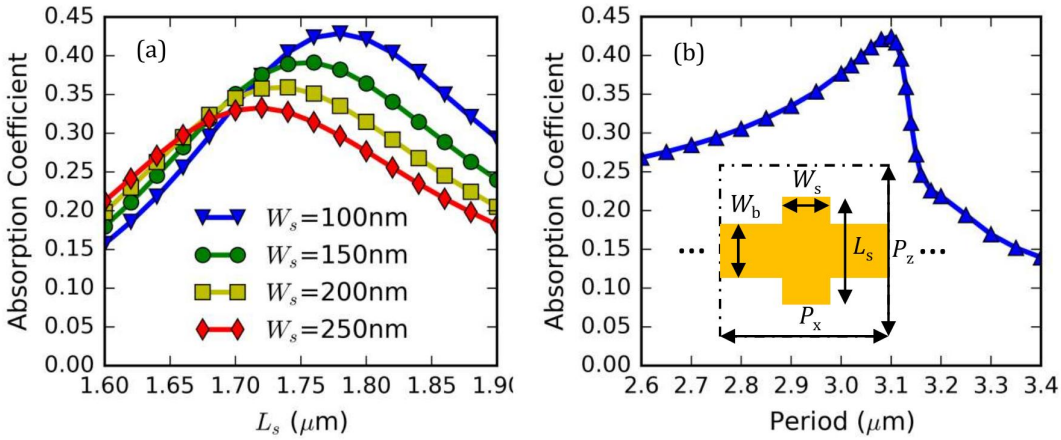

Figure 3. The absorption coefficients as functions (a) of the strip length L_s and strip width W_s for a given period of Px = Pz = 3.1 μm, and (b) of the period for a given strip with L_s = 1.77 μm and W_s = 100 nm. The inset in (b) shows the antenna unit cell in top view. The unit cells are connected in the x direction.

The gap between the suspended nanowire and the substrate is 350 nm based on the waveguide thickness. However, this value can be easily shifted due to fabrication. The effect of the gap variation on the absorption coefficient is plotted in Figure 4. The parameters of the antenna unit cell are chosen from the above simulations. When the substrate thickness varies from 250 nm to 450 nm, a ±100 nm variation from the designed value, there are only small fluctuations on the absorption coefficients. For the antenna at 4.3 μm, the maximum variation is 7% compared to the absorption coefficient at gap = 350 nm. Since the fabrication induced error will be less than 100 nm, the effect of the gap variation on the absorption coefficient will be negligible.

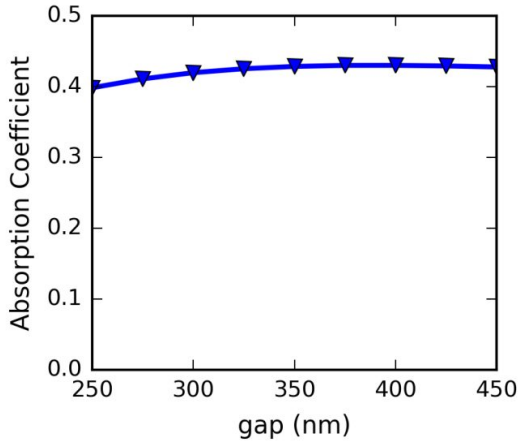

Figure 4. The absorption coefficient as a function of the gap between the nanowire and the substrate for the antenna unit cell at 4.3 μm. The antenna unit cell in (a) has L_s = 1.77 μm, W_s = W_b =100 nm, and P_x = P_z = 3.1 μm.

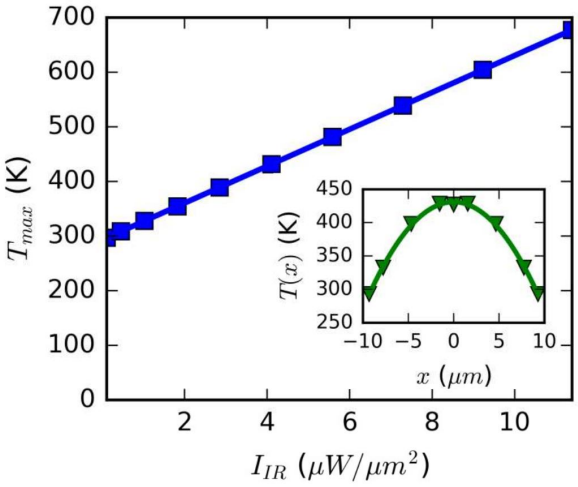

Figure 5. The maximum temperature of the nanowire as a function of the IR power density. The inset shows the temperature profile along the nanowire when the input power density is 4 μW/μm^2.

For demonstration purpose, we design a fishbone nanowire that includes 6 strip antenna unit cells. The total length of the wire, l = 18.6 μm, is selected as a compromise of fabrication challenges and the amount of deflection of the wire. The two ends of the nanowire are connected to the metal pads which act as heat sinks, and the temperature of the two ends are then set to be 293.15 K. The heat transfer coefficient on the wire surface is assigned to be 5 W/(m^2·K) to mimic the stagnant air cooling condition. For a 4 μW/μm^2 normal incident power density (z-polarized) at 4.3 μm wavelength, the highest temperature on the nanowire can reach 428.16 K, and the temperature profile along the nanowire is quasi-parabolic as depicted in the inset of Figure 5. Figure 5 also illustrates that the maximum temperature T_{max} on the nanowire increases linearly with respect to the incident power density. The slope of the curves indicates that the temperature-IR power density conversion ratio η_{TI} is 33.75 K/(μW/μm^2) for this device. The displacement-temperature

conversion ratio, η_{DT}, is estimated to be 0.17 nm/K based on the parabolic temperature profile, meaning that a 1 K temperature increment in the beam center will elevate the nanobeam center by 0.17 nm

2.4 Nanowire Array Optimization

The fishbone nanowires are periodically arranged along the waveguide direction (the *z* direction), to form an OLWA and modulate the propagating wave in the waveguide. Instead of measuring the radiation patterns like we did for OLWAs [22], the change of the waveguide output power, $\Delta P_{wg,out}$, at the radiation *on* and *off* states is of interest here, because it is a measurable quantity by an on-chip photo detector. For fair comparison, we normalize the variation of the waveguide output power to its input power, yielding the change of the S_{21} parameter, ΔS_{21}. The number of the nanowires, *N*, affects ΔS_{21} in a way that too few wires limit the modulation strength, while too many wires can attenuate the output power severely, making it challenging to measure ΔS_{21}. From the simulation results, the gap changes from 50 nm to 73.5 nm in the IR radiation *off* and *on* states, a sweep of *N* finds that ΔS_{21} reaches the maximum when *N* equals 9, and the peak value is 0.106, as shown in Figure 6(a), indicating a modulation depth of 10% on the transmitted power in the waveguide. With the chosen wire number *N*=9, the S_{21} as a function of the change of the gap is studied to reveal the sensitivity of S_{21} to the gap variation, η_{SD}, as shown in Figure 6(b). When the gap is 50 nm, 1 nm increment in the gap will result in 4.6×10^{-3} shift in S_{21} parameter.

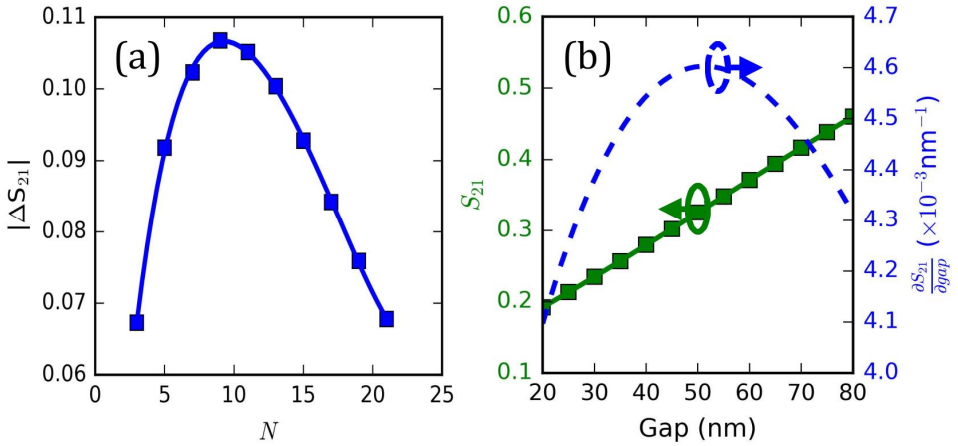

Figure 6. (a) The differences of the S_{21} parameters, ΔS_{21}, at gap = 50 nm and gap = 73.5 nm are plotted as a function of the number of nanowires *N*. (b) S_{21} parameter as a function of the gap is shown as the green curve on the left axis. The derivative of S_{21} with respect to the gap is plotted as the dashed blue curve on the right axis

2.5 Probe Power Limitation

It is worth noting that increasing the waveguide input power can enlarge the output power difference, but it will also heat the nanowire by its own evanescent field, leading to a larger gap than the designed value and desensitizing the detector. Since the waveguide is narrow compared to the nanowire, the waveguide can be viewed as a point heat source, and the temperature profile along the nanowire changes linearly with respect to positions. When the input power is smaller than 100 μW, there will be at most 3.36 nm self-heating deflection, which is an acceptable value.

3. RESPONSITIVITY OF THE DETECTOR

Combining all the conversion ratios from the electromagnetic domain to the thermal domain and then to the mechanical domain and finally back to the optical domain, the figure of merit (FOM) of the device is defined as

$$\mathrm{FOM} = \frac{\partial S_{21}}{\partial I_{IR}} = \eta_{SD}\eta_{DT}\eta_{TI} \tag{4}$$

For the proposed device, its FOM is 2.64×10^{-2} μm^2/μW, indicating that 1 μW/μm^2 radiation will result in 2.64×10^{-2} change in the waveguide S_{21} parameter.

The FOM of the device is given as a more generic performance metric, because the probe light power P_{probe} and device area A_{DUT} have been normalized to get rid of their effects. Thus, only the waveguide S_{21} parameter (normalized to the probe light power) and IR power density (normalized to the device area) are considered. Here, we will convert the FOM ($\mu m^2/\mu W$) to the response of the detector (V/W) to make a fair comparison. Suppose we have a photodetector, which can convert the ac components of the power from the waveguide into current, followed by a transimpedance amplifier to convert the current to the voltage. The photodetector has a responsivity η_{PD} = 0.886 A/W, and the transimpedance amplifier has a resistance, R_{IV}, of 10^5 V/A. These values are adopted from Ref. [17]. Then the response of our detector is

$$\eta_{DUT} = \frac{V_{out}}{P_{IR}} = \frac{FOM}{A_{DUT}} \cdot P_{probe} \cdot \eta_{PD} \cdot R_{IV} \tag{5}$$

where A_{DUT} is the device area and it equals 18.6 μm × 3.1 μm × 9 = 518.94 μm^2. Then $\eta_{\text{PD}} = 2.64\times10^{-2}$ ($\mu m^2/\mu W$) /518.94(μm^2) × 100 μW ×0.886 A/W ×10^5 V/A = 450.7 V/W.

4. CONCLUSIONS

In summary, we propose an on-chip bimetallic plasmo thermomechanical mid-IR detector that uses waveguided modes to detect IR incident wave through the evanescent field modulation. The design is scalable and can be applied to wavelengths from mid-IR to near-IR. FOM is used to characterize the device performance, but it can also be converted to the responsivity in the unit of V/W. We estimate our device performance to be ~450.7 V/W, comparable to the work in Ref. [17] given the same system parameters, but with an advantage of 1/10 smaller probe light power and on-chip integration capability. This manuscript reports the proof-of-the-concept device not targeting to compete with the state-of-the-art semiconductor photo detectors. Although we focus on the readout from the guided modes in this paper, it is also possible to detect the readout through the free space radiation by the leaky waves.

5. ACKNOWLEDGMENT

This work is supported by a grant of the National Science Foundation ECCS 1449397 SNM.

REFERENCES

[1] A. Rogalski, "Infrared detectors: status and trends," *Prog. Quantum Electron.*, vol. 27, no. 2–3, pp. 59–210, 2003.
[2] Z. J. Coppens, W. Li, D. G. Walker, and J. G. Valentine, "Probing and Controlling Photothermal Heat Generation in Plasmonic Nanostructures," *Nano Lett.*, vol. 13, no. 3, pp. 1023–1028, Mar. 2013.
[3] N. J. Hogan, A. S. Urban, C. Ayala-Orozco, A. Pimpinelli, P. Nordlander, and N. J. Halas, "Nanoparticles Heat through Light Localization," *Nano Lett.*, vol. 14, no. 8, pp. 4640–4645, Aug. 2014.
[4] Y. Li, T. Ono, and M. Esashi, "Bimetallic Thermal Radiation Microsensor with Integrated Dipole Antenna," in *TRANSDUCERS 2007 - 2007 International Solid-State Sensors, Actuators and Microsystems Conference*, 2007, pp. 1939–1942.
[5] G. Sebald, E. Lefeuvre, and D. Guyomar, "Pyroelectric energy conversion: Optimization principles," *IEEE Trans. Ultrason. Ferroelectr. Freq. Control*, vol. 55, no. 3, pp. 538–551, Mar. 2008.
[6] J. P. Carmo, L. M. Goncalves, and J. H. Correia, "Thermoelectric Microconverter for Energy Harvesting Systems," *IEEE Trans. Ind. Electron.*, vol. 57, no. 3, pp. 861–867, Mar. 2010.
[7] J. B. Herzog, M. W. Knight, and D. Natelson, "Thermoplasmonics: Quantifying Plasmonic Heating in Single Nanowires," *Nano Lett.*, vol. 14, no. 2, pp. 499–503, Feb. 2014.
[8] M. R. Watts, M. J. Shaw, and G. N. Nielson, "Optical resonators: Microphotonic thermal imaging," *Nat. Photonics*, vol. 1, no. 11, pp. 632–634, Nov. 2007.
[9] J. Zhu, S. Ozdemir, and L. Yang, "Infrared light detection using a whispering-gallery-mode optical microcavity," *Appl. Phys. Lett.*, vol. 104, no. 17, p. 171114, Apr. 2014.
[10] T. W. Kenny, W. J. Kaiser, S. B. Waltman, and J. K. Reynolds, "Novel infrared detector based on a tunneling displacement transducer," *Appl. Phys. Lett.*, vol. 59, no. 15, pp. 1820–1822, Oct. 1991.

[11] F. Zhang *et al.*, "Infrared Detection Based on Localized Modification of Morpho Butterfly Wings," *Adv. Mater.*, vol. 27, no. 6, pp. 1077–1082, Feb. 2015.
[12] H. Zhu, F. Yi, and E. Cubukcu, "Plasmonic metamaterial absorber for broadband manipulation of mechanical resonances," *Nat. Photonics*, vol. 10, no. 11, pp. 709–714, Nov. 2016.
[13] J. R. Barnes *et al.*, "A femtojoule calorimeter using micromechanical sensors," *Rev. Sci. Instrum.*, vol. 65, no. 12, pp. 3793–3798, Dec. 1994.
[14] J. Lai, T. Perazzo, Z. Shi, and A. Majumdar, "Optimization and performance of high-resolution micro-optomechanical thermal sensors," *Sens. Actuators Phys.*, vol. 58, no. 2, pp. 113–119, Feb. 1997.
[15] M. Toda, T. Ono, F. Liu, and I. Voiculescu, "Evaluation of bimaterial cantilever beam for heat sensing at atmospheric pressure," *Rev. Sci. Instrum.*, vol. 81, no. 5, p. 055104, May 2010.
[16] R. Lefevre *et al.*, "Numerical study of bimetallic actuated micro-membrane with large deformations," *J. Micromechanics Microengineering*, vol. 23, no. 1, p. 015011, 2013.
[17] F. Yi, H. Zhu, J. C. Reed, and E. Cubukcu, "Plasmonically Enhanced Thermomechanical Detection of Infrared Radiation," *Nano Lett.*, vol. 13, no. 4, pp. 1638–1643, Apr. 2013.
[18] J. Agustí Batlle and G. Abadal Berini, *Nonlinear micro/nano-optomechanical oscillators for energy transduction from IR sources*. Universitat Autònoma de Barcelona, 2015.
[19] G. A. Magel, "Integrated optic devices using micromachined metal membranes," in *Proc. SPIE 2686, Integrated Optics and Microstructures III,* 1996, vol. 2686, pp. 54–63.
[20] Q. Zhao, Y. Huang, C. Guclu, F. Capolino, and O. Boyraz, "Optical Leaky Wave Antenna Experiment Demonstration and Electronic Modulation Investigation," in *CLEO*, 2015, p. JTh2A.43.
[21] Q. Zhao, C. Guclu, Y. Huang, S. Campione, F. Capolino, and O. Boyraz, "Experimental demonstration of directive Si3N4 optical leaky wave antennas with semiconductor perturbations at near infrared frequencies," in *Proc. SPIE 9365, Integrated Optics: Devices, Materials, and Technologies XIX*, 2015, vol. 9365, p. 93651K–93651K–10.
[22] Q. Zhao, C. Guclu, Y. Huang, F. Capolino, and O. Boyraz, "Experimental Demonstration of Directive Si3N4 Optical Leaky Wave Antennas With Semiconductor Perturbations," *J. Light. Technol.*, vol. 34, no. 21, pp. 4864–4871, Nov. 2016.
[23] Q. Zhao, P. Sadri-Moshkenani, M. W. Khan, R. Torun, I.-U. Zaman, and O. Boyraz, "Infrared Detection Using Plasmonically Enhanced Thermomechanically Actuated Nanowire Arrays," in *Conference on Lasers and Electro-Optics (2017), paper JTh2A.114*, 2017, p. JTh2A.114.
[24] Q. Zhao, P. Sadri-Moshkenani, M. W. Khan, R. Torun, and O. Boyraz, "On-Chip Bimetallic Plasmo-Thermomechanical Detectors for Mid-Infrared Radiation," *IEEE Photonics Technol. Lett.*, vol. 29, no. 17, pp. 1459–1462, Sep. 2017.
[25] J. F. Bauters *et al.*, "Ultra-low-loss high-aspect-ratio Si3N4 waveguides," *Opt. Express*, vol. 19, no. 4, pp. 3163–3174, Feb. 2011.
[26] D. Dai, J. Bauters, and J. E. Bowers, "Passive technologies for future large-scale photonic integrated circuits on silicon: polarization handling, light non-reciprocity and loss reduction," *Light Sci. Appl.*, vol. 1, no. 3, p. e1, Mar. 2012.
[27] Y. Huang, Q. Zhao, L. Kamyab, A. Rostami, F. Capolino, and O. Boyraz, "Sub-micron silicon nitride waveguide fabrication using conventional optical lithography," in *Advanced Photonics for Communications*, 2014, p. JT3A.27.
[28] Y. Huang, Q. Zhao, L. Kamyab, A. Rostami, F. Capolino, and O. Boyraz, "Sub-micron silicon nitride waveguide fabrication using conventional optical lithography," *Opt. Express*, vol. 23, no. 5, pp. 6780–6786, Mar. 2015.
[29] Q. Liu *et al.*, "Highly sensitive Mach–Zehnder interferometer biosensor based on silicon nitride slot waveguide," *Sens. Actuators B Chem.*, vol. 188, pp. 681–688, Nov. 2013.
[30] Q. Zhao, Y. Huang, R. Torun, S. Rahman, T. C. Atasever, and O. Boyraz, "Numerical investigation of silicon nitride trench waveguide," in *SPIE*, 2015, vol. 9586, p. 95860O–95860O–8.
[31] Q. Zhao, Y. Huang, and O. Boyraz, "Optical properties of V-groove silicon nitride trench waveguides," *J. Opt. Soc. Am. A*, vol. 33, no. 9, pp. 1851–1859, Sep. 2016.
[32] A. R. Johnson *et al.*, "Chip-based frequency combs with sub-100 GHz repetition rates," *Opt. Lett.*, vol. 37, no. 5, p. 875, Mar. 2012.
[33] R. Halir, Y. Okawachi, J. S. Levy, M. A. Foster, M. Lipson, and A. L. Gaeta, "Ultrabroadband supercontinuum generation in a CMOS-compatible platform," *Opt. Lett.*, vol. 37, no. 10, p. 1685, May 2012.

[34] C. G. H. Roeloffzen *et al.*, "Silicon nitride microwave photonic circuits," *Opt. Express*, vol. 21, no. 19, pp. 22937–22961, Sep. 2013.
[35] Q. Zhao, M. Rajaei, and O. Boyraz, "Silicon Nitride on Silicon-on-Insulator: a Platform for Integration Active Control over Passive Components," 2016, p. JW2A.125.
[36] S. Jin, L. Xu, H. Zhang, and Y. Li, "LiNbO3 Thin-Film Modulators Using Silicon Nitride Surface Ridge Waveguides," *IEEE Photonics Technol. Lett.*, vol. 28, no. 7, pp. 736–739, Apr. 2016.
[37] Y. Huang, Q. Zhao, N. Sharac, R. Ragan, and O. Boyraz, "Highly nonlinear sub-micro silicon nitride trench waveguide coated with gold nanoparticles," in *SPIE*, 2015, vol. 9503, p. 95030H–95030H–8.
[38] M. Darvishzadeh-Varcheie, C. Guclu, R. Ragan, O. Boyraz, and F. Capolino, "Electric field enhancement with plasmonic colloidal nanoantennas excited by a silicon nitride waveguide," *Opt. Express*, vol. 24, no. 25, pp. 28337–28352, Dec. 2016.
[39] P.-T. Lin, H.-Y. Chu, T.-W. Lu, and P.-T. Lee, "Trapping particles using waveguide-coupled gold bowtie plasmonic tweezers," *Lab Chip*, vol. 14, no. 24, pp. 4647–4652, 2014.
[40] Q. Zhao, C. Guclu, Y. Huang, F. Capolino, and O. Boyraz, "Plasmon Optical Trapping in Silicon Nitride Trench Waveguide," in *CLEO: Science and Innovations*, 2015, p. JTu5A–80.
[41] Q. Zhao, C. Guclu, Y. Huang, F. Capolino, R. Ragan, and O. Boyraz, "Plasmon optical trapping using silicon nitride trench waveguides," *J. Opt. Soc. Am. B*, vol. 33, no. 6, pp. 1182–1189, Jun. 2016.
[42] Y. Huang *et al.*, "Phase-gradient gap-plasmon metasurface based blazed grating for real time dispersive imaging," *Appl. Phys. Lett.*, vol. 104, no. 16, p. 161106, Apr. 2014.
[43] R. J. Roark and W. C. Young, *Formulas for Stress and Strain*, 5 ed. McGraw-Hill, 1975.
[44] M. Manna, F. Magistrali, M. Maini, and D. Reichenbach, "Finite element method applied to stress simulation of high power 980nm pump lasers," *Microelectron. Reliab.*, vol. 37, no. 10–11, pp. 1667–1670, Oct. 1997.
[45] W. M. Haynes, Ed., *CRC Handbook of Chemistry and Physics*, 97 edition. CRC Press, 2016.
[46] "WebElements Periodic Table»Young's modulus»periodicity." [Online]. Available: https://www.webelements.com/periodicity/youngs_modulus/.
[47] "WebElements Periodic Table»Linear expansion coefficient»periodicity." [Online]. Available: https://www.webelements.com/periodicity/coeff_thermal_expansion/.
[48] F. Yi, H. Zhu, J. C. Reed, and E. Cubukcu, "Plasmonically Enhanced Thermomechanical Detection of Infrared Radiation," *Nano Lett.*, p. 130320090705008, Mar. 2013.
[49] J. Kischkat *et al.*, "Mid-infrared optical properties of thin films of aluminum oxide, titanium dioxide, silicon dioxide, aluminum nitride, and silicon nitride," *Appl. Opt.*, vol. 51, no. 28, pp. 6789–6798, Oct. 2012.
[50] A. D. Rakic, A. B. Djurišic, J. M. Elazar, and M. L. Majewski, "Optical Properties of Metallic Films for Vertical-Cavity Optoelectronic Devices," *Appl. Opt.*, vol. 37, no. 22, pp. 5271–5283, Aug. 1998.
[51] "WebElements Periodic Table»Electrical resistivity»periodicity." [Online]. Available: https://www.webelements.com/periodicity/electrical_resistivity/.